Nanoscale Advances

ROYAL SOCIETY OF CHEMISTRY

PAPER

View Article Online
View Journal | View Issue

Cite this: *Nanoscale Adv.*, 2020, **2**, 489

A near infrared dye-coated silver nanoparticle/carbon dot nanocomposite for targeted tumor imaging and enhanced photodynamic therapy†

Rongjun Liu,[ab] Zhengmin Yang,[a] Liangliang Zhang, *[a] Jingjin Zhao, [a] Cheng Hou [a] and Shulin Zhao *[a]

An excellent photosensitizer for imaging-guided high efficiency photodynamic therapy (PDT) requires certain features, such as near-infrared (NIR) light emission, high singlet-to-triplet intersystem crossing (ISC) efficiency, and tumor targeting. However, synthetizing photosensitizers that meet the aforementioned characteristics still remains a challenge. In this study, we synthetized a NIR dye (CyOH)–coated silver nanoparticle/carbon dot nanocomposite (CyOH–AgNP/CD) as a novel nanophotosensitizer for targeted tumor imaging and high-efficiency PDT. The CyOH–AgNP/CD nanophotosensitizer was constructed using a NIR dye (CyOH) and an AgNP/CD nanohybrid *via* Ag–O interaction. Relative to the AgNP/CD nanohybrid, CyOH–AgNP/CD exhibited a high singlet oxygen yield, mitochondrial accumulation, superior tissue penetration of 660 nm laser irradiation, and enhanced tumor targeting. The developed nanophotosensitizer exerted a higher antitumor effect than the CyOH dye or AgNP/CD nanohybrid. This result provides a new idea for the design of excellent photosensitizers that can benefit high-efficiency PDT.

Received 20th September 2019
Accepted 10th December 2019

DOI: 10.1039/c9na00596j

rsc.li/nanoscale-advances

Introduction

Photodynamic therapy (PDT) has recently gained considerable interest owing to its negligible side effects and a high level of efficiency.[1–7] Under irradiation of light with specific wavelengths, photosensitizers generate singlet oxygen ($^1O_2$) that can damage adjacent biomolecules because of strong oxidizing capability, thus inhibiting cancer cell growth. Near-infrared (NIR) light not only acts as a deeply penetrating excitation source but also provides NIR emission signals for fluorescence imaging. A large number of NIR organic dyes have thus far been used as photosensitizers for deep PDT.[8–13] However, single NIR organic dyes have several disadvantages, such as poor water solubility, photo-instability, and short circulation half-life.[14] To overcome these aforementioned disadvantages, new generation nanophotosensitizers were synthesized using a NIR organic dye doped nanomaterial for improved fluorescence imaging and efficient treatment of tumors.[15–18]

An excellent nanophotosensitizer for high efficiency PDT should have at least three features: NIR light emission, high singlet-to-triplet intersystem crossing (ISC) efficiency, and tumor targeting. Decreasing the ΔE_{ST} (energy gap) of nanocomposites can improve the singlet-to-triplet ISC rate, leading to an increase in $^1O_2$ yield.[19–21] Heavy atoms can enhance spin–orbit coupling, which has been proved to increase the ISC rate.[22,23] Therefore, the design and synthesis of a heavy atom-doped nanophotosensitizer can potentially improve the ISC rate and achieve a high $^1O_2$ yield.

Tumor targeting is another important factor for enhancing tumor imaging and PDT efficacy. With enhanced permeability and retention (EPR) effects or/and by modifying with specific ligands, nanophotosensitizers efficiently accumulate in tumor tissues.[24,25] Such accumulation not only enhances tumor imaging and PDT efficacy but also helps minimize phototoxic damage to normal tissues in PDT.[26,27] The mitochondrion, an ideal hypersensitive organelle, generates reactive oxygen species (ROS) and regulates apoptosis.[28–30] If the ROS is generated by PDT in the mitochondrion, the adjacent biomolecules are damaged directly and efficiently, activating the cell apoptosis signaling pathway and accelerating cell death.[31,32] Therefore, the development of new nanophotosensitizers that exhibit high ISC efficiency, tumor-targeting, and mitochondrial accumulation is highly expected for improved imaging guided PDT as well as reduced side effects.

In this study, we synthetized a NIR dye (CyOH)–coated silver nanoparticle/carbon dot nanocomposite (CyOH–AgNP/CD) as a mitochondrion-targeted nanophotosensitizer for targeted tumor imaging and high-efficiency PDT. The designed CyOH–

[a]*State Key Laboratory for the Chemistry and Molecular Engineering of Medicinal Resources, Guangxi Normal University, Guilin, 541004, China. E-mail: liangzhang319@163.com; zhaoshulin001@163.com*

[b]*Guangxi Key Laboratory of Agricultural Resources Chemistry and Biotechnology, Yulin Normal University, Yulin, 537000, China*

† Electronic supplementary information (ESI) available. See DOI: 10.1039/c9na00596j

AgNP/CD nanophotosensitizer consists of two parts. The first part is a NIR dye (CyOH), which not only provides NIR fluorescence for fluorescence imaging but also preferably accumulates in mitochondria because of its structure which includes a quaternary ammonium salt.[11,33] The second part consists of Ag-doped carbon dots referred to as the Ag nanoparticle/carbon dot nanohybrid (AgNP/CD). Coupling of AgNP/CD with the NIR dye (CyOH) led to an increase in water solubility and $^1O_2$ yield. On the basis of prominent photostability and tumor-targeted ability, the CyOH–AgNP/CD nanophotosensitizer also exhibited improved tumor imaging and PDT efficiency.

Results and discussion

Characterization of CyOH–AgNP/CD

The morphologies of the as-prepared AgNP/CD and CyOH–AgNP/CD are characterized by transmission electron microscopy (TEM). Fig. 1A and B present the TEM and high-resolution TEM (HRTEM) images of AgNP/CD, respectively, with spherical diameters ranging from 2 nm to 13 nm. As shown in Fig. 1D and E, the TEM and HRTEM observations of CyOH–AgNP/CD reveal the aggregation of CyOH–AgNP/CD. The labeled planar distance of 0.24 nm was in accordance with the (111) lattice spacing of Ag,[34,35] and amorphous parts corresponded to the CDs. Typical X-ray photoelectron spectroscopy (XPS) (Fig. 1C and F) of AgNP/CD and CyOH–AgNP/CD indicated the presence of three similar peaks corresponding to the elements C, Ag, and O. Compared with AgNP/CD, CyOH–AgNP/CD exhibited a lower Ag content. Meanwhile, CyOH–AgNP/CD exhibited higher contents of C and O.

CyOH was synthesized as described in previous studies,[29,30] and the synthetic route is depicted in Scheme S1.† MS, ^{1}HNMR, and ^{13}C NMR were used to characterize the chemical structures of CyOH (Fig. S1–S3†).

Optical properties of CyOH–AgNP/CD and detection of $^1O_2$

We measured the optical properties of AgNP/CD, CyOH, and CyOH–AgNP/CD. As observed in Fig. 2A, AgNP/CD shows a strong characteristic absorption peak at 420 nm. CyOH had three absorption peaks from 600 nm to 750 nm, with the highest peak at 681 nm, which is consistent with other reports.[36] After CyOH conjugation with AgNP/CD, the emission spectrum of CyOH–AgNP/CD showed four absorption peaks at 420, 625, 681, and 715 nm. Similar results were obtained for AgNP/CD and CyOH, indicating that CyOH was successfully conjugated with AgNP/CD *via* an Ag–O bond. The prepared AgNP/CD, CyOH, and CyOH–AgNP/CD were uniformly and stably stored at room temperature for an extended period without evident precipitation. The solutions were yellow, blue, and green, respectively (Fig. 2A, inset). Fig. 2B shows the fluorescence emission spectra of CyOH and CyOH–AgNP/CD in ethanol/Tris–HCl buffer (1 : 1 v/v, pH 7.4). Under excitation of 633 nm light, their fluorescence maximum emission peak at 723 nm was observed. Compared with that of CyOH, the fluorescence intensity of CyOH–AgNP/CD at 723 nm was reduced. The fluorescence intensity of CyOH–AgNP/CD was very dependent on the pH value of solution (Fig. S4†).

To assess the ability of AgNP/CD, CyOH, and CyOH–AgNP/CD to generate $^1O_2$, we employed DPBF as a $^1O_2$ trapper to detect the generated $^1O_2$ by a change in the intensity of the absorption peaks at 420 nm. In the presence of AgNP/CD (Fig. 2C) under irradiation of a 660 nm laser, the absorbance of DPBF at 420 nm remained unchanged with prolonged irradiation time. However, in the presence of CyOH (Fig. 2D) or CyOH–AgNP/CD (Fig. 2F), the absorbance of DPBF decreased gradually. This result indicates the degradation of DPBF by $^1O_2$ generated by CyOH and CyOH–AgNP/CD. The degradation rate of DPBF resulting from CyOH–AgNP/CD was considerably larger than that from CyOH, indicating that CyOH–AgNP/CD can be used as an efficient nanophotosensitizer for PDT. The degradation rate of CyOH–AgNP/CD was dependent on the pH value of solution (Fig. S5†). Moreover, the generation of $^1O_2$ by CyOH–AgNP/CD under laser irradiation was also proved by the electron spin resonance (EPR) spectroscopy method (Fig. S6†).

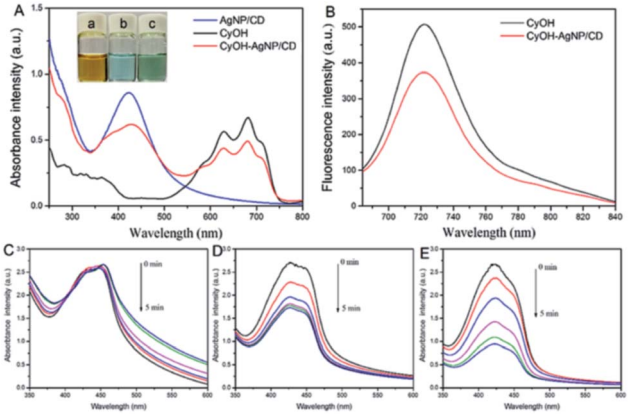

Fig. 2 (A) UV-vis absorption spectra of AgNP/CD, CyOH, and CyOH–AgNP/CD. Inset: photograph of the AgNP/CD, CyOH, and CyOH–AgNP/CD solution under irradiation of natural light. (B) Emission spectra (λ_{ex} = 633 nm) of CyOH and CyOH–AgNP/CD dispersed in ethanol/Tris–HCl buffer (1 : 1 v/v, pH 7.4). The UV-vis absorption spectra of DPBF + AgNP/CD (C), DPBF + CyOH (D), and DPBF + CyOH–AgNP/CD (E) with different irradiation durations by using a 660 nm laser (60 mW cm^{-2}).

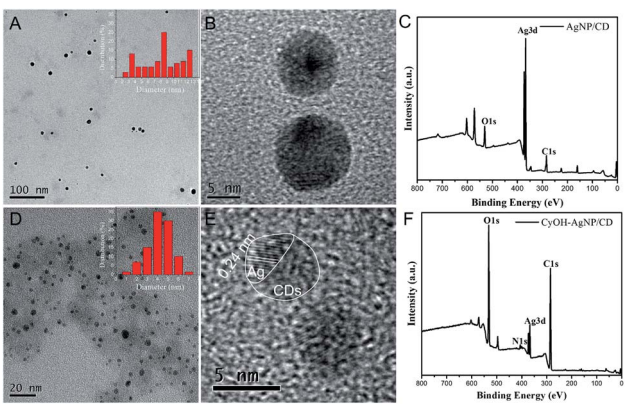

Fig. 1 TEM images (inset shows the size distribution) (A, D), HRTEM images (B, E) and XPS (C, F) of AgNP/CD and CyOH–AgNP/CD.

Mechanism for enhanced $^1O_2$ production and cytotoxicity

To gain insight into the mechanism underlying the increased $^1O_2$ production under NIR illumination, time-dependent density functional theory was employed to calculate ΔE_{ST}. The ΔE_{ST} values of CyOH and CyO–Ag were calculated to be 1.0022 and 0.0429 eV, respectively, with reference to the data in Table S1 and Fig. S7.† Compared with CyOH, CyO–Ag had a lower ΔE_{ST} and thus could increase the ISC rate and improve the yield of $^1O_2$.[16–18] The proposed mechanism is described in Fig. 3.

To evaluate the cytotoxicity of the synthetic AgNP/CD, CyOH, and CyOH–AgNP/CD, we selected the 4T1 cell line (murine breast cancer cell) for testing. The three samples were added to 96-well plates cultured with 4T1 cells at different concentrations (10–400 μg mL^{-1}) for 24 h. The cellular viability was then measured. It was found that the cell viabilities exceeded 80% in the presence of AgNP/CD, CyOH, and CyOH–AgNP/CD (Fig. S8†), indicating their negligible cytotoxicity. However, after laser irradiation, the toxicity of CyOH–AgNP/CD to cells was significantly increased. The cellular viability was approximately 10% after irradiation with a 660 nm laser for 5 min (Fig. S9†).

Mitochondrial accumulation and photoinduced cytotoxicity

To study the subcellular localization of CyOH–AgNP/CD, we used MitoTracker for colocalization experiments (Fig. 4). The green fluorescence from MitoTracker (Fig. 4A) was overlapped with red fluorescence from the CyOH–AgNP/CD probe (Fig. 4B), with an overlap coefficient of 0.80 (Fig. 4C and D). These results confirm that CyOH–AgNP/CD can target the mitochondria. Moreover, the PDT effects of AgNP/CD, CyOH, and CyOH–AgNP/CD on 4T1 cells were verified by calcein-AM and propidium iodide co-staining. After laser irradiation, most cells in the CyOH–AgNP/CD group died (Fig. 4H), proving and reconfirming the improved PDT of 4T1 cells induced by CyOH–AgNP/CD. By contrast, the cells incubated with AgNP/CD and CyOH were only slightly affected by laser irradiation (Fig. 4F and G).

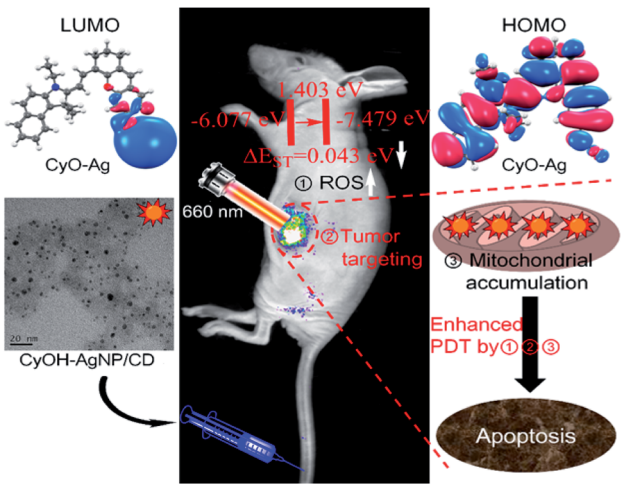

Fig. 3 Mechanism for enhanced $^1O_2$ production and cytotoxicity.

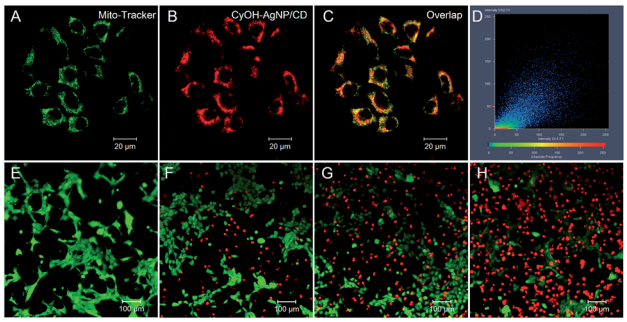

Fig. 4 Colocalization images of the 4T1 cells stained with MitoTracker and CyOH–AgNP/CD (A–D). Green channel: λ_{ex} = 488 nm and λ_{em} = 500–570 nm; red channel: λ_{ex} = 633 nm and λ_{em} = 640–750 nm. Live/dead images of the 4T1 cells with calcein-AM and propidium iodide co-staining in the presence of PBS (E), AgNP/CD (F), CyOH (G), and CyOH–AgNP/CD (H).

Targeted tumor imaging

We investigated the tumor accumulation ability of CyOH and CyOH–AgNP/CD by *in vivo* fluorescence imaging. In the CyOH group (Fig. 5A and C), the NIR fluorescence signals from CyOH at the tumor site gradually increased with time extending, and the fluorescence intensity reached a maximum at 20 h. Nevertheless, in the CyOH–AgNP/CD group (Fig. 5B and D), the fluorescence signal at the tumor site reached its maximum at 24 h post-injection. Owing to its larger size, CyOH–AgNP/CD needs more time to accumulate at the tumor site *via* the EPR effect. Main organs from sacrificed mice were extracted at 36 h post-injection, and then imaged for the biodistribution of CyOH and CyOH–

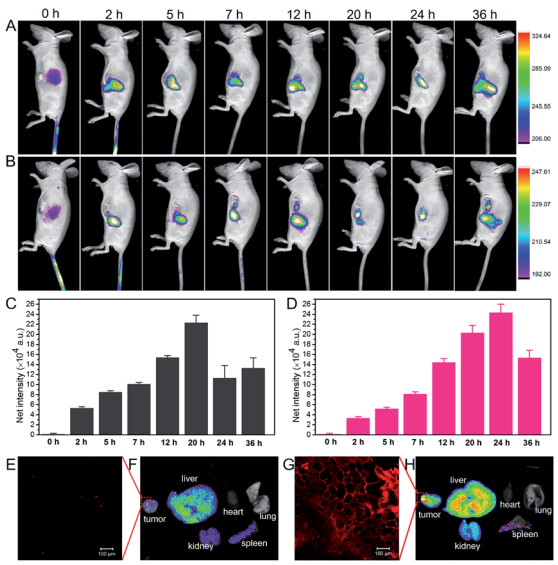

Fig. 5 *In vivo* fluorescence images of CyOH (A) and CyOH–AgNP/CD (B) at different time points after intravenous injection. The fluorescence intensity of tumors with CyOH (C) and CyOH–AgNP/CD (D) at different time points. Confocal fluorescence microscopy image of tumors after treatment with CyOH (E) and CyOH–AgNP/CD (G), λ_{ex} = 633 nm, and λ_{em} = 650–750 nm. Biodistribution of CyOH (F) and CyOH–AgNP/CD (H) in tumor-bearing mice after 36 h.

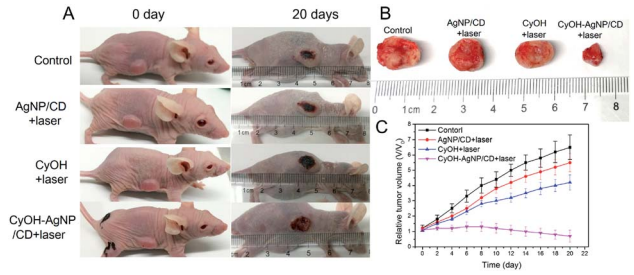

Fig. 6 (A) Photographs of mice before and after treatment for 20 days. (B) Photograph of tumor tissues of sacrificed mice from the four groups after treatment for 20 days. (D) Tumor growth curves of mice in the four groups.

AgNP/CD *in vivo*. The fluorescence intensity in different organs exhibited similar biodistributions in both CyOH (Fig. 5F) and CyOH–AgNP/CD (Fig. 5G), indicating that CyOH and CyOH–AgNP/CD could be selectively delivered to the tumor site on the basis of the EPR effect. Moreover, the fluorescence at the tumor tissue was observed in the confocal fluorescence microscopy image. Fig. 5E shows weak fluorescence for CyOH in the tumor tissue, whereas Fig. 5G presents strong fluorescence for CyOH–AgNP/CD in the tumor tissue. The aforementioned results indicate that the as-prepared CyOH–AgNP/CD exhibits enhanced accumulation in the tumor relative to CyOH.

Antitumor PDT

We evaluated the therapeutic efficacy of CyOH–AgNP/CD on the 4T1 tumor-bearing mice. When the tumor volume in the mice reached the predetermined volume, they were divided into four groups to compare the PDT results. As shown in Fig. 6A–C and S10,† the tumor volume becomes considerably enlarged after PDT for 20 days in the control group. The tumors in the AgNP/CD and CyOH groups were inhibited to a certain extent. However, in the CyOH–AgNP/CD group, apparent tumor shrinkage was observed, which was attributed to its generation of additional $^1O_2$. To confirm the therapeutic efficiency, tumor tissues of the sacrificed mice from the four groups after PDT for 20 days were extracted for H&E staining. H&E-stained images showed few changes in the control group, AgNP/CD-treated group, and CyOH-treated group, whereas the CyOH–AgNP/CD-treated group exhibited severe destruction of the tumor tissue (Fig. S11†). Meanwhile, H&E-stained images of main organs (heart, liver, spleen, and kidney) of the sacrificed mice from the four groups are shown in Fig. S12.† As can be seen, H&E-stained images of tissue slides for the main organs from control, AgNP/CD, CyOH and CyOH–AgNP/CD groups all showed few changes. These results demonstrate that CyOH–AgNP/CD exerted limited side effects on the main organs of mice.

Conclusions

In summary, we synthesized a CyOH–AgNP/CD nanocomposite as a new nanophotosensitizer for simultaneously improved tumor imaging and PDT. The developed nanophotosensitizer exhibited excellent properties, such as stable NIR fluorescence, good biocompatibility, negligible toxicity, and selective accumulation in tumors. Compared with free CyOH, CyOH–AgNP/CD can not only target tumors but also generate more $^1O_2$ by reducing its ΔE_{ST}. Owing to its tumor imaging ability and significant antitumor effect, CyOH–AgNP/CD exhibits potential for future clinical imaging-guided PDT.

Experimental

Synthesis of CyOH

CyOH was synthesized using a method described in previous studies.[33,37] Prior to CyOH synthesis, compound **3** as an intermediate was prepared from compound **1** and compound **2** by following the synthetic route depicted in Scheme S1.† The purified compound **3** (1.0 g), resorcinol (1.7 g), and anhydrous *N*,*N*-dimethylformamide (DMF, 15 mL) were then added into a two-neck vessel. The mixture was heated to 115 °C under a dry N_2 atmosphere for 2 h. After the temperature was cooled to room temperature, the solvents were removed using a rotary evaporator. Yield: 45.6 mg (60%). ^{1}H NMR (DMSO-d6, 400 MHz, Fig. S1†) δ: 8.70 (dd, J = 15.0 Hz, 1H), 8.35 (d, J = 8.5 Hz, 1H), 8.20 (d, J = 8.9 Hz, 1H), 8.15 (d, J = 8.0 Hz, 1H), 7.93 (d, J = 8.9 Hz, 2H), 7.74 (t, J = 8.3 Hz, 1H), 7.62 (t, J = 7.3 Hz, 2H), 7.50 (s, 1H), 7.47 (d, J = 8.5 Hz, 1H), 6.94 (d, J = 2.0 Hz, 2H), 6.86 (dd, J = 2.0, 8.5 Hz, 2H), 6.55 (d, J = 15.0 Hz, 1H), 4.54 (d, J = 7.2 Hz, 2H), 2.72 (m, 4H), 2.00 (s, 6H), 1.85 (m, 2H), 1.44 (t, J = 7.1 Hz, 3H). ^{13}C NMR (DMSO-d6, 100 MHz, Fig. S2†) δ: 178.27, 162.17, 161.01, 154.66, 144.33, 139.26, 136.01, 134.24, 132.67, 131.24, 130.51, 129.65, 128.53, 127.67, 126.40, 126.30, 122.95, 114.88, 114.09, 112.70, 103.45, 102.52, 52.38, 28.82, 27.55 (2C), 24.07, 20.52, 13.35. MS (Fig. S3†) m/z calcd for $C_{31}H_{30}NO_2^+$ $[M]^+$, 448.2; found, 448.1.

Preparation of CDs

By using citric acid as a precursor, CDs with reducing properties were prepared *via* a hydrothermal method. Citric acid (1.0 g) was mixed in water (25 mL) under vigorous stirring. The solution was transferred to a Teflon-lined autoclave and then reacted for 8 h at 200 °C. When the solution was cooled to room temperature, the obtained liquid was adjusted with a 1 M NaOH solution to pH = 7.0. A purified CD solution was ultimately obtained using a dialysis bag (1000 Da) for 6 h.

Preparation of AgNP/CD

The aforementioned solution (5 mL) containing reduced CDs was adjusted to pH = 8.0–9.0 by adding a NaOH (70 mM) solution. Approximately 500 μL of a 140 mM $AgNO_3$ solution was added with magnetic stirring. After the reaction for 6 h at room temperature, a yellow-brown AgNP/CD solution was obtained.

Preparation of CyOH–AgNP/CD

The CyOH–AgNP/CD nanocomposites were synthesized using CyOH and AgNP/CDs *via* Ag–O bond interaction. First, 0.5 mg CyOH was dissolved in a 4 mL ethanol/Tris–HCl buffer solution (pH = 7.4, 1 : 1, v/v), and 1 mL of AgNP/CDs (10 mg mL^{-1}) was mixed with the CyOH solution. The mixture was subsequently

stirred and shaken uniformly to obtain a CyOH–AgNP/CD nanocomposite solution.

Detection of singlet oxygen

Diphenylbenzofuran (DPBF) as a trapping agent was applied to detect $^1O_2$. The prepared CyOH, AgNP/CD, and CyOH–AgNP/CD solutions were added into the DPBF ethanol solution (10 mM) sequentially, and the mixture was exposed to a 660 nm laser (60 mW cm^{-1}). The absorption intensity of DPBF at 420 nm for each sample was detected by UV-visible (UV-vis) absorption spectrometry.

Confocal imaging for colocalization

4T1 cells were seeded on a 35 mm glass-bottomed culture dish. When ~75% confluency was reached, 10 μM CyOH–AgNP/CD was added. After co-incubation for 8 h, free CyOH–AgNP/CD was removed by washing with RPMI 1640 three times. These cells were incubated with MitoTracker for 30 min, followed by colocalization imaging.

Targeted tumor imaging

Animal handling procedures were approved by the Animal Ethics Committee of Guangxi Normal University (No. 20150325-XC). Breast cancer tumors were obtained by subcutaneous injection of 4T1 cells (100 μL, ~5×10^6) into nude mice. CyOH and CyOH–AgNP/CD (100 μL, 1.5 mg kg^{-1}) were intravenously injected in the mice, sequentially. These mice were then anesthetized and scanned using a Kodak FX-Pro imaging system for long-term monitoring of the distribution and metabolism of CyOH and CyOH–AgNP/CD.

Antitumor photodynamic therapy

The prepared 4T1 tumor xenografts (with a tumor volume of ~200 mm^3) were divided into four groups: the control group, AgNP/CD-administered and irradiated group (AgNP/CD group), CyOH-administered and irradiated group (CyOH group) and CyOH–AgNP/CD-administered and irradiated group (CyOH–AgNP/CD group). CyOH–AgNP/CD solutions (100 μL, 2 mg mL^{-1}) were injected intravenously into the mice. About 24 h after the photosensitizer was administered, the tumor xenografts were irradiated using a 660 nm laser (60 mW cm^{-1}) for 10 min. The tumor volumes of all mice were measured and recorded during PDT. These mice were ultimately sacrificed, and their tumor xenografts were evaluated by histological examination (hematoxylin and eosin (H&E) staining).

Conflicts of interest

There are no conflicts of interest to declare.

Acknowledgements

This work was supported by the National Natural Science Foundation of China (21575031 and 21874030), Natural Science Foundation of Guangxi Province (2015GXNSFDA139006) and BAGUI Scholar Program.

Notes and references

1 S. Monro, K. L. Colón, H. Yin, J. Roque, P. Konda, S. Gujar, R. P. Thummel, L. Lilge, C. G. Cameron and S. A. McFarland, *Chem. Rev.*, 2019, **119**, 797–828.
2 X. Li, S. Lee and J. Yoon, *Chem. Soc. Rev.*, 2018, **47**, 1174–1188.
3 X. Li, N. Kwon, T. Guo, Z. Liu and J. Yoon, *Angew. Chem., Int. Ed.*, 2018, **57**, 11522–11531.
4 M. Li, J. Xia, R. Tian, J. Wang, J. Fan, J. Du, S. Long, X. Song, J. W. Foley and X. Peng, *J. Am. Chem. Soc.*, 2018, **140**, 14851–14859.
5 Y. Huang, Q. L. Liu, Y. Q. Wang, N. He, R. F. Zhao, J. Choo and L. X. Chen, *Nanoscale*, 2019, **11**, 12220–12229.
6 D. H. Lin, T. Qin, Y. Wang, X. Sun and L. X. Chen, *ACS Appl. Mater. Interfaces*, 2014, **6**, 1320–1329.
7 W. Zhang, Y. Wang, X. Sun, W. Wang and L. X. Chen, *Nanoscale*, 2014, **6**, 14514–14522.
8 A. E. O'Connor, W. M. Gallagher and A. T. Byrne, *Photochem. Photobiol.*, 2009, **85**, 1053–1074.
9 Y. H. Moon, S. M. Kwon, H. J. Kim, K. Y. Jung, J. H. Park, S. A. Kim, Y. J. Kwan, H. P. Jong, A. K. Soo, C. K. Yong, G. A. Sang and J. H. Yoon, *Oncol. Rep.*, 2009, **22**, 1085–1091.
10 J. Atchison, S. Kamila, H. Nesbitt, K. A. Logan, D. M. Nicholas, C. Fowley, J. Davis, B. Callan, A. McHale and J. F. Callan, *Chem. Commun.*, 2017, **53**, 2009–2012.
11 H. W. Liu, X. X. Hu, K. Li, Y. Liu, Q. Rong, L. Zhu, L. Yuan, F. L. Qu, X. B. Zhang and W. Tan, *Chem. Sci.*, 2017, **8**, 7689–7695.
12 M. J. Cook, I. Chambrier, S. J. Cracknell, D. A. Mayes and D. A. Russell, *Photochem. Photobiol.*, 1995, **62**, 542–545.
13 N. Patel, P. Pera, P. Joshi, M. Dukh, W. A. Tabaczynski, K. E. Siters, M. Kryman, R. R. Cheruku, F. Durrani, J. R. Missert, R. Watson, T. Y. Ohulchanskyy, E. C. Tracy, H. Baumann and R. K. Pandey, *J. Med. Chem.*, 2016, **59**, 9774–9787.
14 V. Saxena, M. Sadoqi and J. Shao, *J. Photochem. Photobiol., B*, 2004, **74**, 29–38.
15 S. Gao, P. Zheng, Z. Li, X. Feng, W. Yan, S. Chen, W. Guo, D. Liu, X. Yang, S. Wang, X. J. Liang and J. Zhang, *Biomaterials*, 2018, **178**, 83–94.
16 D. Chen, Q. Tang, J. Zou, X. Yang, W. Huang, Q. Zhang, J. Shao and X. Dong, *Adv. Healthcare Mater.*, 2018, **7**, 1701272.
17 Q. Li, X. Li, L. Zhang, J. Zuo, Y. Zhang, X. Liu, L. Tu, B. Xue, Y. Chang and X. Kong, *Nanoscale*, 2018, **10**, 12356–12363.
18 F. Chen, Z. Zang, Z. Chen, L. Cui, Z. Chang, A. Ma and M. Zheng, *Biomaterials*, 2019, **214**, 119226.
19 E. Ju, K. Dong, Z. Chen, Z. Liu, C. Liu, Y. Huang, Z. Wang, F. Pu, J. Ren and X. Qu, *Angew. Chem., Int. Ed.*, 2016, **128**, 11639–11643.
20 Y. Yuan, C. J. Zhang, R. T. Kwok, S. Xu, R. Zhang, J. Wu, Z. Tang and B. Liu, *Adv. Funct. Mater.*, 2015, **25**, 6586–6595.

21 W. Wu, D. Mao, S. Xu, F. Hu, X. Li, D. Kong and B. Liu, *Chem*, 2018, **4**, 1937–1951.
22 L. Zhou, S. Wei, X. Ge, J. Zhou, B. Yu and J. Shen, *J. Phys. Chem. B*, 2012, **116**, 12744–12749.
23 N. Macia, R. Bresoli-Obach, S. Nonell and B. Heyne, *J. Am. Chem. Soc.*, 2018, **141**, 684–692.
24 C. Han, A. Zhang, Y. Kong, N. Yu, T. Xie, B. Dou, K. Li, Y. Wang, J. Li and K. Xu, *Anal. Chim. Acta*, 2019, **1067**, 115–128.
25 Y. Huang, N. He, Y. Wang, D. Z. Shen, Q. Kang, R. F Zhao and L. X. Chen, *J. Mater. Chem. B*, 2019, **7**, 1149–1159.
26 R. Tang, J. Xue, B. Xu, D. Shen, G. P. Sudlow and S. Achilefu, *ACS Nano*, 2015, **9**, 220–230.
27 Y. Cao, H. Dong, Z. Yang, X. Zhong, Y. Chen, W. Dai and X. Zhang, *ACS Appl. Mater. Interfaces*, 2016, **9**, 159–166.
28 G. Kroemer and J. C. Reed, *Nat. Med.*, 2000, **6**, 513.
29 X. Tan, S. Luo, L. Long, Y. Wang, D. Wang, S. Fang, Q. Ouyang, Y. Su, T. Cheng and C. M. Shi, *Adv. Mater.*, 2017, **29**, 1704196.
30 S. Luo, X. Tan, S. Fang, Y. Wang, T. Liu, X. Wang, Y. Yuan, H. Sun, Q. Qi and C. M. Shi, *Adv. Funct. Mater.*, 2016, **26**, 2826–2835.
31 T. Xiao, J. K. Fan, H. L. Huang, J. F. Gu, L. Y. Li and X. Y. Liu, *Cell Res.*, 2010, **20**, 367.
32 C. Lee, H. K. Park, H. Jeong, J. Lim, A. J. Lee, K. Y. Cheon and S. H. Kim, *J. Am. Chem. Soc.*, 2015, **137**, 4358–4367.
33 L. Yuan, W. Lin, S. Zhao, W. Gao, B. Chen, L. He and S. A. Zhu, *J. Am. Chem. Soc.*, 2012, **134**, 13510–13523.
34 S. Chen, X. Hai, X. W. Chen and J. H. Wang, *Anal. Chem.*, 2014, **86**, 6689–6694.
35 W. Shao, X. Liu, H. Min, G. Dong, Q. Feng and S. Zuo, *ACS Appl. Mater. Interfaces*, 2015, **7**, 6966–6973.
36 C. Han, H. Yang, M. Chen, Q. Su, W. Feng and F. Li, *ACS Appl. Mater. Interfaces*, 2015, **7**, 27968–27975.
37 S. J. Li, C. Y. Li, Y. F. Li, J. Fei, P. Wu, B. Yang and S. X. Nie, *Anal. Chem.*, 2017, **89**, 6854–6860.